



Aerodynamic Shape Design of Pantograph Network Monitoring Device on High-Speed Trains

P. Ji¹, F. Wu^{1,2†}, B. Qian¹ and L. Yan²

¹ Key Laboratory of Traffic Safety on Track, Ministry of Education, School of Traffic & Transportation Engineering, Central South University, Changsha, Hunan, 410075, China

² CRRC Qingdao Sifang CO., LTD, Qingdao, Shandong, 266111, China

†Corresponding Author Email: gszxcfd_wf@csu.edu.cn

(Received August 23, 2018; accepted December 26, 2018)

ABSTRACT

The pantograph monitoring device on high-speed trains bears not only its own strength but also the aerodynamic load applied by the air flow when the train is running at high speed. A well designed shape of the pantograph monitoring device on high-speed trains reduces the loads and pressure fluctuations acting on it, and therefore, increases its function stability and life cycle. In this paper, we present an aerodynamic shape design method for such device. Firstly, an efficient and reliable numerical simulation approach is established for the evaluation of the aerodynamic loads acting on the device. According to the numerical computations, a basic shape for the monitoring device is formed, with which the minimum functional space of the device is reserved. Then, the corners of the basic shape are smoothed out with three types of continuous transitions. By comparing the numerical results of the three smoothed shapes, we obtain an optimal aerodynamic shape for the pantograph monitoring device. The design method is not limited to the monitoring device studied in this manuscript. The aerodynamic shape of other small functional devices on high-speed trains can also be generated or optimized with the method presented herein.

Keywords: Pantograph monitoring device; Aerodynamic performance; Numerical simulation; Shape design.

NOMENCLATURE

C_d	force coefficient	ρ	air density
F_x	the aerodynamic drag force	V	operation speed of train
h	characteristic height	S	reference area
P	pressure		

1. INTRODUCTION

With the development of high-speed railway, the catenary electrified railway has been popularized. The high-speed trains throughout the world are mainly powered by electrified railway system (Miao *et al.*, 2014). The pantograph, which connects the power grid with the vehicle, plays a key role in the proper functioning of the high-speed railway system (Sun, 2011). To ensure the liability of vehicle pantograph system, a device installed on the train roof is used for real-time monitoring,

status feedback, and troubleshooting of pantograph-catenary faults (shown in Fig. 1). The device uses infrared thermal imaging detection technology to monitor the running status between the contact net, the pantograph, and the bow net in real time. The data is then transmitted to the control center. Once the received data exceeds the safety threshold of the railway operation requirement, alarm will be automatically triggered and reported to safeguard the operating train. (Li, 2018).

Meanwhile, the working conditions of pantograph and catenary gets more severe (Xu *et al.*, 2014) with the increase of train speed. The aerodynamic effect with



Fig. 1. Train pantograph network monitoring device.

the monitoring device on the roof becomes more significant under high speed condition (Bruni *et al.*, 2018). On the other hand, the aerodynamic design of the train directly affects the normal work and the service life of the device (Liu *et al.*, 2018). Therefore, the shape of the pantograph monitoring device is particularly important in train aerodynamic performance.

Previous studies on the pantograph monitoring system emphasizes the device functionality and artistic features in design stage (Liu *et al.*, 2018; Marta *et al.*, 2017; Chen, 2016; GU, 2013). Aerodynamic features of the device do not receive much attention until the end stage of the device design, when the device shape is slightly optimized based on its aerodynamic performance (Zhou *et al.*, 2015; Branke *et al.*, 2008; Li *et al.*, 2016). With this design process, the aerodynamic feature of the device is not involved in topological structure innovation (Tian, 2007). However, for multi-objective shape optimization along the entire design phase, design iteration allows only little change on the topological relationship of the original scheme. Therefore, it is difficult to improve the aerodynamic performance of the device with many restrictive conditions after the design optimization. The devices were fixed on the roof of the car in groups and it is difficult to analyze using wind tunnel test. Meanwhile, there are limited resources such as manpower, capital and devices can be invested in the development of the monitoring device. Hence, it is more feasible to re-design the device with consideration of aerodynamic analysis. It is hard to get full vehicle 3D data in experiments due to the conflict of limited experimental time and massive response data. Based on the discussions above, numerical simulation is the most efficient method for this study. The numerical simulations are combined with the conventional shape design method to form a new design approach.

Main purpose of the shape design and optimization of the high-speed trains is to

reduce the load brought by the aerodynamic drag of the train under the high speed condition within given constraints such as the interior geometry, the manufacturing process, and the topological features of the device (Xu *et al.*, 2014). The early aerodynamic optimization design is “droplet” shaped, where the symmetric line on the train follows the pattern of the outer surface of a falling droplet. The front and rear shapes of the optimized device are made up of curved but smooth three-dimensional surfaces (Hyun *et al.*, 2017). These curved smooth 3D surface streamlines are designed using CAD technology. Compromise must be made between the curvature details on each surface and the data transfer effectiveness during the CAD design stage (Zhang *et al.*, 2017b). In this study, we use the 3D design software CATIA™ to build and optimize geometric models. In this software, the 3D surfaces can be built and adjusted based on the design requirements. There are four types of transition control for the surface connection (G0 to G4). The contour line in the model is controlled by the non-uniform rational B-spline (NURBS) curves, and the three-dimensional curved surface is generated by the NURBS surfaces. The models build by CATIA™ is then transferred into finite volume analysis software ANSYS Fluent® for aerodynamic analysis. The aerodynamic features of the device will be optimized based on the simulation results.

Since the monitoring devices were fixed on the train, the flow field around the device is also affected by other geometries around it. Numerical simulation with the device model only may lead to inaccurate solutions. Meanwhile, it is impractical to establish experimental measurements for the pantograph device on the train model due to the concern of limited budget and measurement precision. The finite volume simulation approach could effectively avoid the limitations mentioned above. Therefore, various simulation models regarding different model geometry and computational domain were established and studied. The model with best precision and efficiency will be provided in the conclusion as a guidance for shape design of the pantograph (Miao *et al.*, 2014).

In this study, we established a shape design method for the monitoring device that combines reliable aerodynamic simulations with traditional design

approach. This design method is not limited to the design of the monitoring device studied in this manuscript. The aerodynamic shape of other small functional devices on high-speed trains can also be generated or optimized with the method presented herein.

2. COMPUTATION OF AERODYNAMIC LOADS ON THE MONITORING DEVICE

2.1. Geometric Model

Realistically, the pantograph monitoring devices are fixed on the roof of high-speed trains in pairs, and each pair of devices is located symmetrically about the middle plane of the train (see Fig. 1). In order to establish a numerical method for the computation of aerodynamic performance of the device with acceptable computational cost and minimum numerical error, three numerical simulation models are established: single device model, roof model, and full train model.

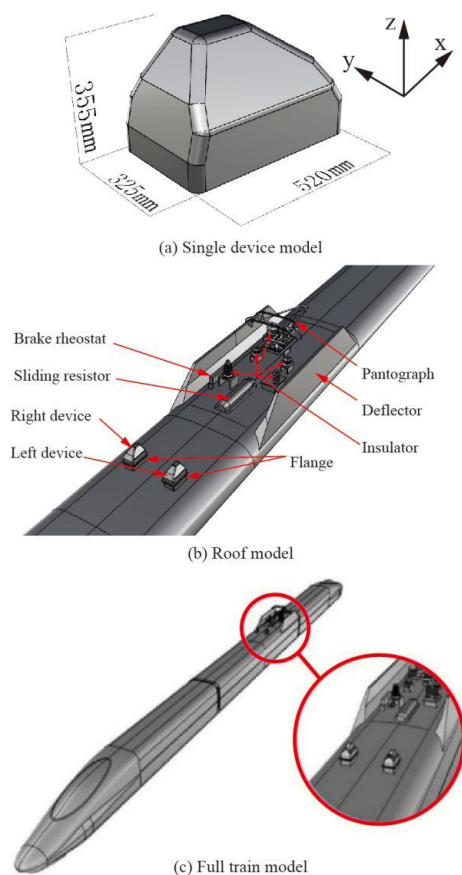


Fig. 2. Computation Models.

We use CATIA™ to create the geometric models. As shown in Fig. 2(a), the single device model considers the device itself only, by

ignoring the aerodynamic effects from the train body and the pantograph. For the roof model, it is assumed that the flow field of the monitoring device is affected by the surrounding devices on the train roof, which produces different flow environment around the device. The roof model neglects the influence of the train body on the devices, it only focuses on the influence of the roof geometries on the devices. The devices are placed on the roof of the train together with the pantograph and surrounding devices according to the actual assembly conditions (see Fig. 2(b) for details). Figure 2(c) demonstrates the full train model, in which the monitoring devices and other devices are fixed on the roof of a full scaled train. This model restores the real working condition of the monitoring devices as much as possible, and considers the aerodynamic loads on the devices with the presence of train, pantograph and other devices. The full train model consists of three cars. The monitoring devices are placed on the roof according to the actual assembly conditions. Note that for the roof model and full train model, the device on the negative y-axis is named as the left device, and the other one is named as the right device.

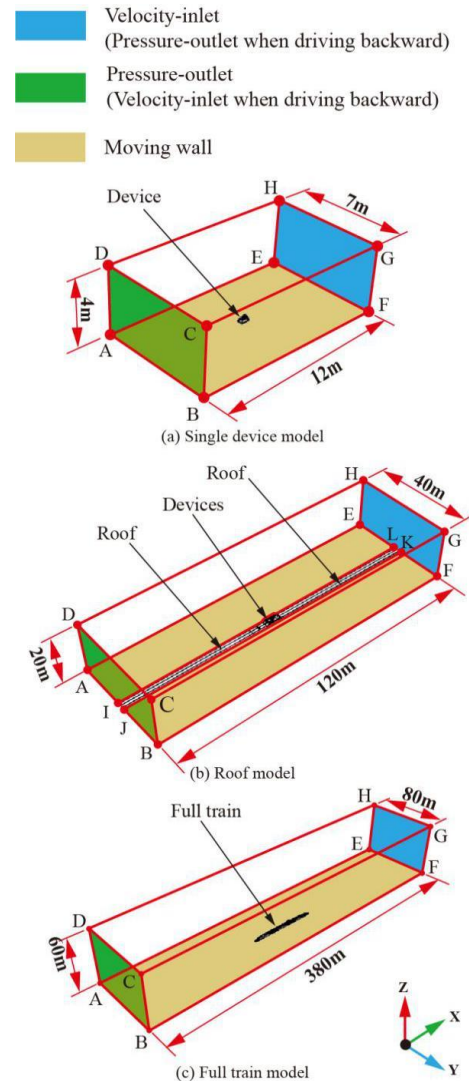


Fig. 3. Computational domains of the three models.

2.2. Computational Domain and Boundary Conditions

According to the numerical study of the external flow around high-speed trains in (Zhang *et al.*, 2015), the computational model is located in the center of the computational domain. In order to reduce the flow acceleration caused by the blocking effect of the model on the computational domain, the blocking ratio between the model and computational domain is limited to be less than 2%. (Chen *et al.*, 2017; EN 14067-4, 2009) Thus, height of the domain should be no less than 10 times of the characteristic height (h) of the computational model, and the width of the domain should be no less than 20 times of the computational model (Chen *et al.*, 2017; Zhang *et al.*, 2017a).

Define the train running along the negative x -axis to be forward driving, and along the positive x -axis to be backward driving. The train is located in the middle of the computational domain, and the distance from the device to the boundaries perpendicular to x -axis is roughly $30h$. The calculation domains are created according to the specific dimensions of the three sets of models introduced in Sect. 2.1, and shown in Fig. 3.

To simulate the operation of trains, it is usually assumed that the train is stationary, and the air blows into the computational domain in the opposite direction with the same speed (Tian, 2007; Tan *et al.*, 2018). Referring to Fig. 3, the entrance boundary is set to be the air flow entrance boundary (face ABCD), and the speed is given by the actual operation speed of 350 km/h. Static pressure on the pressure outlet (face EFGH) is equal to ambient pressure (0 Pa in simulations). The bottom of the computational domains (face ABEF for the single device model and full train model, and face AILE and face GBFK for the roof model) is set as moving wall, and the moving velocity is identical to the air from the inlet to realize the relative motion between ground and train (Tan *et al.*, 2018). When the simulated train travels in the along x direction, the velocity inlet and the pressure outlet boundary conditions are switched accordingly. The direction of the moving wall boundary condition also needs to be adjusted accordingly.

2.3. Numerical Schemes

The numerical simulations in the current manuscript is conducted in ANSYS Fluent. When describing the relative motion of the model, the air flow around the object must obey the laws of conservation of physics, as well as the additional turbulent transport equation. The laws of conservation of physics consists of the mass conservation, the momentum conservation, and the energy conservation (Zhang *et al.*, 2015) For the turbulent transport

equation, Fluent provides a variety of turbulence models. The RNG $k-\epsilon$ turbulence model, widely used for engineering applications, is adopted herein. (Li *et al.*, 2017; Zhang *et al.*, 2017b; Rogowski *et al.*, 2018).

2.4. Computational Grid and Mesh Convergence

The computational domain of the single device model is discretized with structured meshes. Averaged size of the surface mesh is 25mm. Thickness of the first layer mesh is 1mm, and the growth rate is 1.15. The space discretization method is established and applied to the other two computational domains (roof model and full train model). Due to the complex structure near the pantograph area and bogies area, hybrid meshing is used for the roof model and full train model, that is, unstructured mesh for the pantograph area and bogies area and structured mesh for the rest. In the complex area near the pantograph and bogies, an unstructured grid with a size of 30mm is used as shown in Fig. 4.

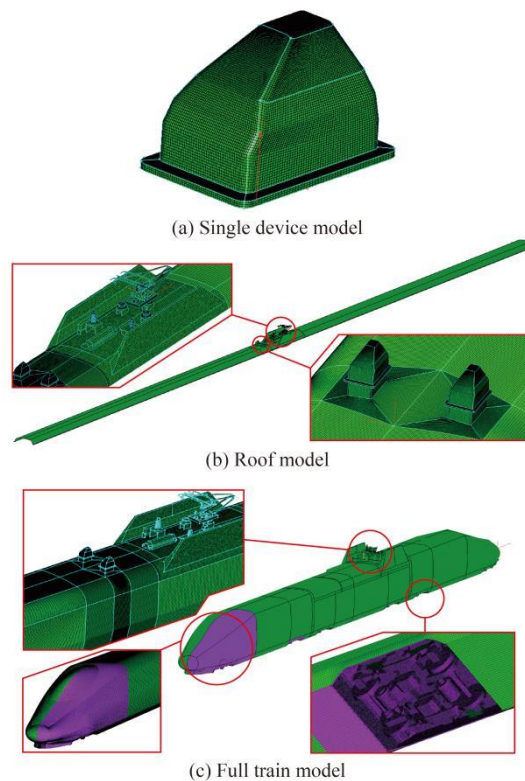


Fig. 4. Mesh of models.

Table 1 shows the comparison of the mesh information for the three computation models. The single device model has the smallest number of grid cells, while the full train model possesses the largest number of grids, which is 23.41million.

The single device model is selected for the mesh convergence test, as it requires the minimum computational power. Thickness of the first layer mesh is 1mm, and the growth rate is 1.15, which is referred as the medium mesh. For the mesh independence tests, fine mesh and coarse mesh are created with reference to the medium mesh as in Fig. 5. The growth rate for fine mesh and coarse mesh are 1.05 and 1.2, respectively. The numerical simulations for mesh convergence test

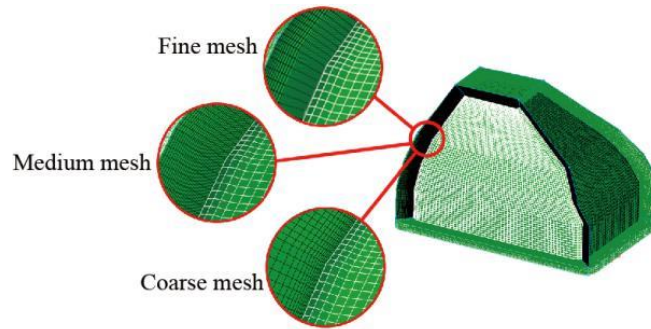


Fig. 5. Mesh model.

are carried out with a train speed of 350km/h. The drag coefficients of the three sets of grids are calculated using the following Eq. (1):

$$C_d = \frac{F_x}{0.5\rho V^2 S} \quad (1)$$

Table 1 Mesh information for different computation models

Model	Number of Cells (million)
Single device model	4.01
Roof model	8.57
Full train model	23.41

Where F_x represents the aerodynamic drag force, ρ represents air density, V represents the operation speed of train, and S is the device reference area, which is set to be $0.935m^2$ in the current study. Table 2 presents the numerical results from different meshes. Relative error is defined as the percentage of the difference from the Medium mesh result. One can see from table 2 that the results of the three grids are quite close.

Table 2 Aerodynamic drag acting on the device for different mesh sizes

Mesh Case	Fine mesh	Medium mesh	Coarse mesh
Number of Mesh Cell (million)	5.61	4.01	2.74
Drag coefficient	0.42	0.407	0.39
Relative error	3.2%	\	4%

Additionally, Fig. 6 shows the distribution of

wall Y plus on the device. The value of wall Y plus is mostly between 30 and 150, which satisfies the requirement of the RNG k- ϵ turbulence model. Thus, it is reasonable to use the medium mesh for the rest of numerical simulations in this study.

2.5. Experimental Verification

In order to verify the simulation method and grid layout of this paper, a new calculation is carried out, and the results are compared with the results of wind tunnel test. The test was conducted in a high-speed test section of a wind tunnel at the National Engineering Laboratory for High Speed Railway Construction. The cross-sectional area of the test section is $3 \times 3 m^2$, the length of the test section is 15 m. (Niu *et al.*, 2017)

Our numerical simulation uses the identical setup as this test. According to Niu's experiment, we establish a two-car formation train geometric model (scaled at 1:20). Then the previous grid layout settings are used to discretize the geometric model, as Fig. 7. Comparison of the experimental test and numerical simulation are presented in table 3 (Niu *et al.*, 2016). The pressure distribution of the two-car formation train is shown in Fig. 8.

According to the data comparison in Table 3, the numerical simulation results of the drag coefficient agree well with the experimental results. Maximum relative error is 5.5%. Thus, it can be concluded that the numerical method and mesh used introduced above are reliable.

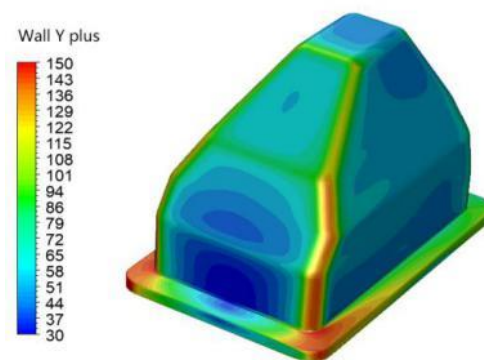


Fig. 6. Distribution of wall Y plus on the device.

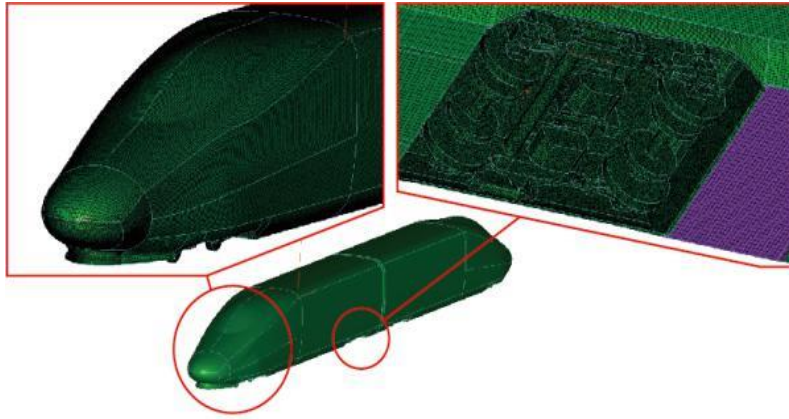


Fig. 7. Mesh for Verification.

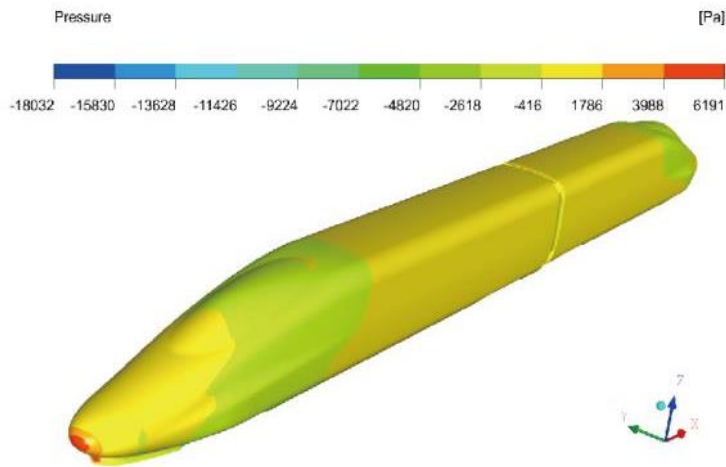


Fig. 8. Pressure distribution of verification model.

Table 3 Comparison of experimental and numerical coefficient of drag on the train

	Position	Cd	Relative error
Experimental (Niu. <i>et al.</i> , 2016)	Head car	0.113	\
	Tail car	0.146	\
Numerical	Head car	0.107	5.3%
	Tail car	0.138	5.5%

2.6. Numerical Result

In the current study, the train runs in two directions at a speed of 350 km/h. The numerical results of the aerodynamic drag of the device are shown in Table 4. It can be concluded that the drag on the device in all models is similar in the forward driving scenario. In the roof model and full train model, the device is affected by the boundary layer of the roof surface. However, since the device is installed on a mounting base of 230mm in height on the roof, the device is not completely submerged in the boundary layer. Thus, in the

forward driving scenario, the drag coefficients of the two models are relatively close and slightly smaller than that of the single device model. In the backward driving scenario, flow around the monitoring devices is significantly disturbed by the roof devices, such as the pantograph and accessory devices upstream, the aerodynamic drag on the monitoring devices are obviously smaller than that in the forward driving scenario.

The surface pressure distribution on devices for all computational models are shown in Fig. 9, from which it can be observed that the pressure distribution for the roof model is similar to that for the full train model, while that for the single device model is quite different

Table 4 Aerodynamic drag coefficients on the device of different models

Scenario	Device	Forward driving case	Backward driving case
Single device model	One device	0.407	0.413
Roof model	Right device	0.405	0.353
	Left device	0.391	0.205
Full train model	Right device	0.401	0.324
	Left device	0.387	0.203

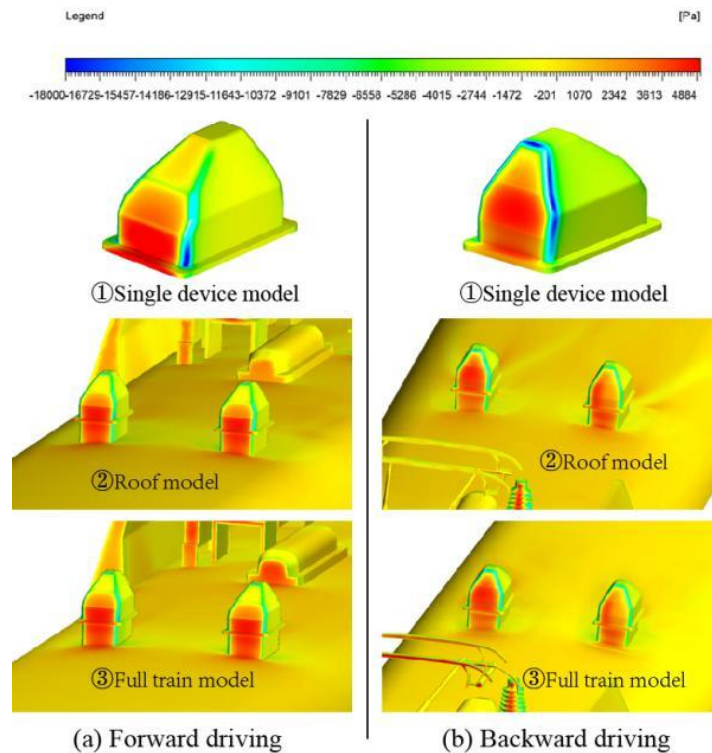


Fig. 9. Pressure distribution on the devices for different computational models.

from the others. Especially in the backward driving scenario, flow around the monitoring devices for the roof model and the full train model are perturbed by other devices, and a non-uniform positive pressure distribution appears on the front of the right device. The negative pressure zone between the front and side of the device is much stronger for the single device model as the device is up against the air flow directly in this case.

Figure 10 shows the surface pressure curve of the symmetry plane of the device. The y-axis is the surface pressure value acting on the device, and the x-axis is the distance D between the position of measuring point and the starting point P in the lower left corner. Comparing to other models, the pressure amplitude of the windward surface for the single device model is larger, and that of the leeward surface is smaller. The single device model involves the least amount of vehicle data and occupied computing resources, but the simulation results

differ greatly from other models. Especially for backward driving case. Numerical results of the roof model is well agreed with that of the full train model. However, the required computational power for the roof model is significantly less than that for the full train model. Thus, the numerical approach established in this section, i.e. the roof model discretized with the medium mesh, is used for the following design and simulations.

3. SHAPE DESIGN OF THE MONITORING DEVICE

3.1. Design of the Windward Shape

To reduce the air resistance and surface pressure acting on the device, our primary objective of shape design is to reduce the windward area of the monitoring device and optimize the side profile according to the numerical results presented above. The surface modeling software CATIA™ is used for the current design work. The green shaded area in Fig. 11 is the functional space that

needs to be reserved during shape design, in which the corners are marked with point 1 to 10 and the profile is named as C1. In this view, inside the red dash line circle is the detection range of the device sensor. The overlapping part of the scope and the device needs to be equipped with flat glass, to avoid refraction of light. Compared with the original profile line L1, C1 reduces the projected area in the train operational direction by 24.5%. By stretching curve C1 spatially, we obtain a three-dimensional curved surface, namely called S1.

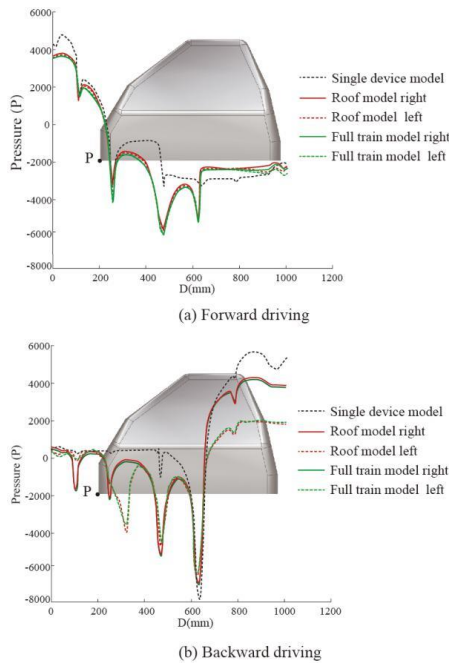


Fig. 10. Curve of pressure change along the shape line on the middle plane of the monitoring device. x-axis is the distance to point P.

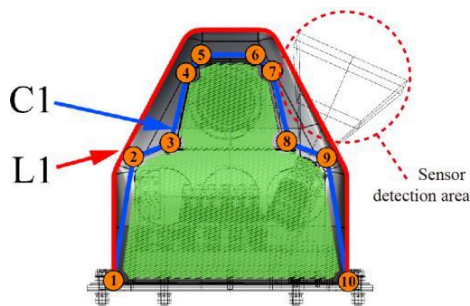


Fig. 11. Front view of the monitoring device.

3.2. Design of the Side Shape

According to the velocity distribution on the middle plane of the device shown in Fig. 12, there is exists large flow separation zone on the top of the device. Combining Fig. 10 and Fig. 12, flow around the device is not smooth due to the sharp changes of the windward and leeward

surfaces, resulting in significant pressure variations at each turning point of the device surface. Consequently, thickness of the device shell needs to be increased due to high risk of material fatigue under alternative aerodynamic loads. Similar to section 3.1, the minimum functional area is shown in Fig. 13 and the corners are marked with points 11 to 20. By connecting the marked points with B-spline, a continuous curve C2 is obtained. By stretching C2 in the transverse direction, we obtain a three-dimensional curved surface called S2.

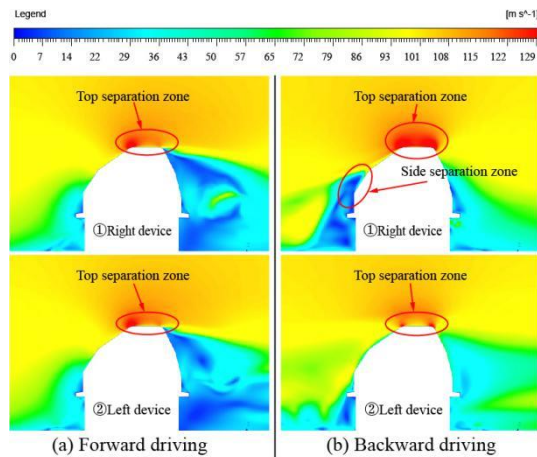


Fig. 12. Velocity distribution on the middle plane of monitoring device.

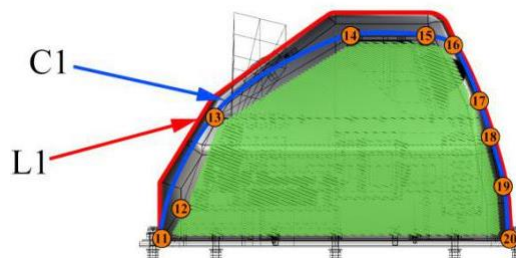


Fig. 13. Side view of the monitoring device.

3.3. Smoothing of the Device Corners

Surfaces S1 and S2 intersect in space, yielding in the basic shape shown in Fig. 14. The sharp corners formed by intersections potentially cause serious flow separations and pressure fluctuations. Thus, it is necessary to carry out the smoothing treatment for the sharp corners. The intersection of S1 and S2 is smoothed with G0, G1, and G2 transitions (right panels in Fig. 14). As introduced in (Tian, 2007), the G0 transition is continuous along a straight line, G1 is continuous up to the first order derivative, and G2 is continuous up to the second order derivative at the junction, i.e. the curvature continuous transition.

3.4. Comparison of Designed Models

3.4.1. Aerodynamic Drag Acting on the Device

Numerical simulations on the designed models, G1,

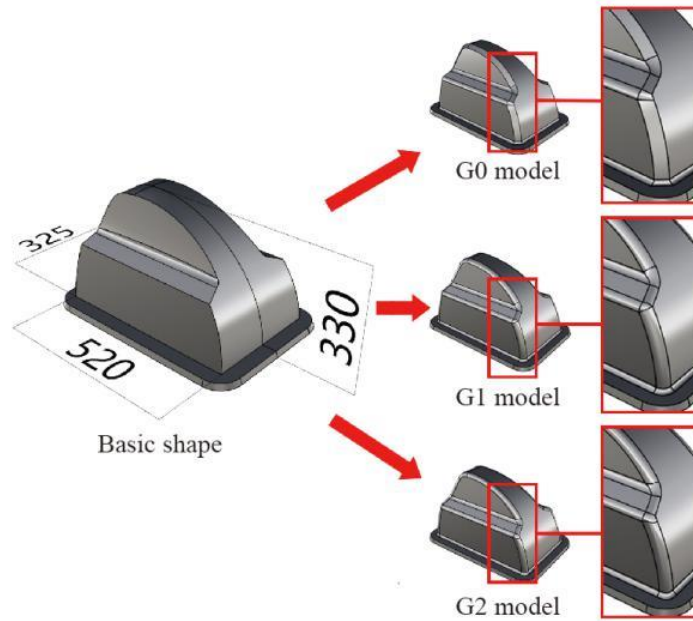


Fig. 14. Basic and smoothed models of the monitoring device.

Table 4 Aerodynamic drag of the device at 350km/h

Model	Device	Forward driving scenario	Backward driving scenario
Original	Right device	0.405	0.353
	Left device	0.391	0.205
G0	Right device	0.341	0.317
	Left device	0.337	0.195
G1	Right device	0.341	0.316
	Left device	0.335	0.194
G2	Right device	0.338	0.321
	Left device	0.332	0.194

G2, and G3, are carried out with the numerical approach established previously. The train operates in the forward and backward direction with speed of 350km/h. As shown in Table 4, difference in the aerodynamic drag of the new designed devices in each operational direction is within 1%. However, comparing to the original model, the drag acting on the new designed device models is significantly reduced in both forward and backward driving scenarios. Maximum drag reduction is roughly 16%, which occurs during forward driving as the area against the incoming air flow on the device is reduced to the minimum.

3.4.2. Surface Pressure Distribution

Demonstrated in Fig. 15 is the pressure

variation along the surface in the middle plane of the device. In general, magnitudes of the pressure variations on the new designed models are smaller than that on the original model. The smoothing treatment on the surface of the new designs significantly reduces the number of pressure fluctuations, such as region A and B marked in Fig. 15. As the flow is not affected by surrounding equipment, pressure variations are similar for both the left and right devices, while those are obviously different for the train driving in the opposite direction.

3.4.3. Velocity Distribution

Since the previous results of aerodynamic drag and pressure distribution on the devices failed to provide effective information for the selection of the three design models, the velocity distribution near the device

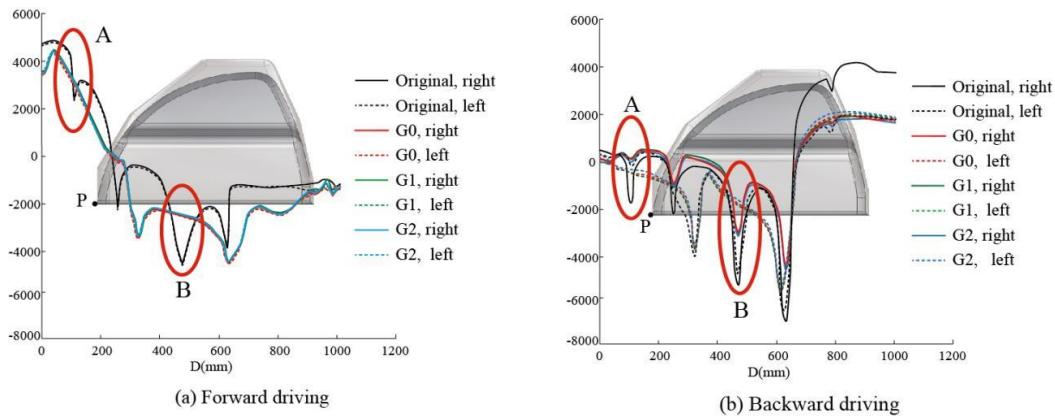
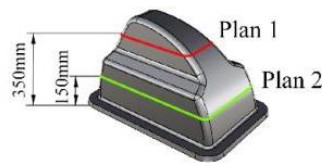
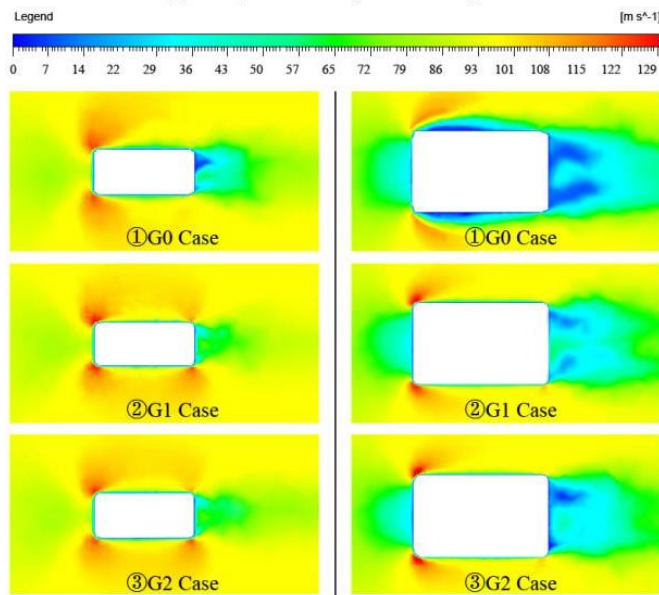


Fig. 15. Comparison of surface pressure variation between the original and designed devices.



(a) The positions of plane 1 and plane 2



(b) Velocity distribution on plane 1

(c) Velocity distribution on plane 2

Fig. 16. Velocity distribution near the device in forward driving scenario.

in the forward driving scenario is shown in Fig. 16 for the investigation of effects of the transition corners, i.e. G0, G1, and G2 smoothing treatments. Plane 1 and Plane 2 are horizontal planes of 350 mm and 150mm above the train roof, respectively. One can see from Fig. 16 that the G0 transition causes a large region of flow separation on both sides and back of the device, where the velocity magnitude drops significantly. For the G1 and G2 cases, the velocity distribution does not differ obviously. Both corner transitions are able to guide the air flow to pass around the

device smoothly without causing intensive flow separation. In the sense, G1 and G2 transitions have similar influence on the air flow around the device, that is, both G1 and G2 designs are acceptable for the optimization of device geometry.

However, take the factors of geometry modeling and engineering manufacture into consideration, the G1 transition for the new designed device model is much simpler than the G2 transition. Therefore, the model with G1 transition is the most optimal shape design scheme for the pantograph monitoring device.

4. CONCLUSION

Due to the wide use of external devices on rail vehicles, this paper proposes an numerical simulation guided aerodynamic shape design method for the generation of optimal device geometry. By combining the validated aerodynamic simulations with shape design, the method of creating the minimum smooth shape is established. It is also found that the transitions between curved surfaces needs to be continuous up to the first order derivative for the purpose of reducing flow separation.

Although the design method proposed in this manuscript is a mixture of existing methods, the focus is to show the application of aerodynamic analysis onto shape design of auxiliary devices, which is not popular in previous studies due to the lack of a precise and efficient numerical computation approach. Through the test of computational models, we proofed that the train roof model with devices installed on is sufficient for the aerodynamic computation of the devices on train roof, instead of using the entire train model. This significantly reduces the computational grids and power required to achieve the same level of numerical precision.

This study contributes to the design and optimization of small functional devices on rail vehicles in the condition of complex flows.

5. ACKNOWLEDGMENTS

The authors would like to acknowledge the financial support from the National Key R&D Program of China (Grant number 2017YFB1201103).

REFERENCES

- Branke, J., K. Deb, K. Miettinen and R. Słowiński (2008). Multiobjective optimization. *Microwave Magazine IEEE* 12 (6) :120-133.
- Bruni, S., Bucca, G., Carnevale, M., Collina, A., and Facchinetti, A. (2018). Pantograph-catenary interaction: recent achievements and future research challenges. *International Journal of Rail Transportation* 6(2), 57-82.
- EN 14067-4. (2009). *Railway Applications - Aerodynamics - Part 4: Requirements and Test Procedures for Aerodynamics on Open Track*. European Committee for Standardization. Brussels Belgium.
- Chen, X. L. (2016). Analysis and design of the appearance characteristics of mechanical equipment. *Sciences & Wealth* 10, 464-465.
- Chen, Z. W., T. H. Liu, Z. H. Jiang, Z. J. Guo and J. Zhang (2017). Comparative analysis of the effect of different nose lengths on train aerodynamic performance under crosswind. *Journal of Fluids And Structures* 78, 69-85.
- Gu, Y. H. (2013). Study on appearance design method of dredging vehicle based on modeling aesthetics. *Journal of Design Machine* 7, 121-123.
- Hyun, K. H., J. H. Lee and M. Kim (2017). A comparative study of methods to simulate aerodynamic flow beneath a high-speed train. *Journal of Intelligent Manufacturing* 28(7), 1729-1741
- Li, H. K. (2018).Application of Vehicle Mounted Catenary Running State Detecting Device (3C).*Telecom Power Technology* 35(6).
- Li, R., P. Xu, Y. Peng and P. Ji (2016). Multi-objective optimization of a high-speed train head based on the FFD method. *Journal of Wind Engineering & Industrial Aerodynamics* 152, 41-49.
- Li, Z. W., M. Z. Yang, S. Huang and X. F. Liang (2017). A new method to measure the aerodynamic drag of high-speed trains passing through tunnels. *Journal of Wind Engineering & Industrial Aerodynamics* 171(2017), 110-120.
- Liu, Z. G., Y. Song, Y. Han, H. G. Wang, J. Zhang and Z. W. Han (2018). Advances of research on high-speed railway catenary. *Journal of Modern Transportation* 26(1), 1-23.
- Marta, P. M., Saeema, A. K., Per B. B., and Hideyoshi, Y. (2017). Investigating the influence of product perception and geometric features. *Research in Engineering Design* 28(3), 357-379.
- Miao, X., L. Zhang, Z. Li, G. Gao and X. Zeng (2014). Aerodynamic performance of train passing out tunnel under cross-wind. *Journal of Central South University* 45(3), 958-964.
- Niu, J. Q., X. F. Liang and D. Zhou (2016).Experimental study on the effect of Reynolds number on aerodynamic performance of high-speed train with and without yaw angle. *Journal of Wind Engineering & Industrial Aerodynamics* 157(2016), 36-46.
- Niu, J. Q., Zhou, D., Liang, X. F.(2017).Experimental research on the aerodynamic characteristics of a high-speed train under different turbulence conditions. *Experimental Thermal and Fluid Science* 80(2017), 117-125.
- Rogowski, K., M. O. L. Hansen and P. Lichota (2018).

- 2-D CFD Computations of the Two-Bladed Darrieus-Type Wind Turbine. *Journal of Applied Fluid Mechanics* 11(4),835-845.
- Sun, L. (2011). Method of Aesthetic Principle-based Outside Design of Petroleum Machinery. *Journal of Oil And Gas Technology* 2011(2), 158-160.
- Tan, X. M., Z. G. Yang, X. L. Wu and J. Zhang (2018). Vortex structures and aeroacoustic performance of the flow field of the pantograph. *Journal of Sound and Vibration* 432,17-32.
- Tian, H. Q. (2007). *Train Aerodynamics*. China Railway Press. Beijing.
- Xu, L. Z., X. F. Liang, T. H. Liu and X. H. Xiong (2014). Pressure variation test inside full-scale high-speed train running in open area. *Journal of Central South University (Science and Technology)* 45(8), 2878- 2884.
- Zhang, J, Gao, G. J., Liu T. H., and Li, Z. W. (2015). Crosswind stability of high speed trains in special cuts. *Journal of Central South University* 22(7), 2849-2856.
- Zhang, L., Yang, M. Z., Liang, X. F. and Zhang, J. (2017a). Oblique tunnel portal effects train and tunnel aerodynamics based on moving model tests. *Journal of Wind Engineering & Industrial Aerodynamics* 167, 128-139.
- Zhang, L., Liu, H., Stoll, N., and Thurow, K. (2017b). Influence of tunnel aerodynamic effects by slope of equal-transect ring oblique tunnel portal. *Journal of Wind Engineering & Industrial Aerodynamics* 169, 106-116.
- Zhou, H. Y., S. Chen, D. Z. Qi and Y. F. Ai (2015). Research on mechanical equipment modeling design based on sheet metal technology. *Journal of Machine Design* 10, 119-121.